Materials Chemistry and Physics 170 (2016) 154–161

Contents lists available at ScienceDirect

Materials Chemistry and Physics

journal homepage: www.elsevier.com/locate/matchemphys

Oxygen deficiency in MoO_3 polycrystalline nanowires and nanotubes

Ana Varlec [a, *], Denis Arčon [a, b], Srečo D. Škapin [c], Maja Remškar [a]

[a] Condensed Matter Physics, Jožef Stefan Institute, Jamova 39, SI-1000 Ljubljana, Slovenia
[b] Faculty of Mathematics and Physics, University of Ljubljana, Jadranska cesta 19, SI-1000 Ljubljana, Slovenia
[c] Advanced Materials Department, Jožef Stefan Institute, Jamova 39, SI-1000 Ljubljana, Slovenia

HIGHLIGHTS

- Polycrystalline MoO_3 nanowires were obtained via oxidation of $Mo_6S_2I_8$ nanowires.
- Nanowires are porous and tubular with either filled or empty interior.
- Nanowires are slightly oxygen deficient which leads to a new Raman band.

ARTICLE INFO

Article history:
Received 16 June 2015
Received in revised form
29 November 2015
Accepted 19 December 2015
Available online 30 December 2015

Keywords:
Defects
Electron resonance
Oxides
Nanostructures
Raman spectroscopy and scattering

ABSTRACT

We report on the synthesis of polycrystalline molybdenum oxide (MoO_3) nanowires via oxidation of molybdenum-sulfur-iodine ($Mo_6S_2I_8$) nanowires. This unique synthesis route results in an interesting morphology comprising porous nanowires and nanotubes. We found the nanowires to have the orthorhombic MoO_3 structure. The structure is slightly oxygen deficient which results in the appearance of a new resonant Raman band (1004 cm^{-1}) and paramagnetic defects (Mo^{5+}) of both the point and crystallographic shear plane nature.

1. Introduction

Molybdenum trioxide, MoO_3, is an important representative of transition metal oxides that are semiconductors with a wide energy band gap. Because of their structural, optical and electronic properties, these materials are used in numerous fields; in photovoltaics [1], gas sensing [2], photo- and electro-chromic applications [3], for intercalation of lithium or hydrogen ions [4] and others. Recently, MoO_3 was shown to be efficient also in applications that benefit from its antibacterial properties [5]. Applications are importantly influenced by crystalline structure, defects and morphology of MoO_3 [2,5].

In addition to three polymorphs of stoichiometric MoO_3, i.e., orthorhombic α-MoO_3, monoclinic β-MoO_3 and hexagonal h-MoO_3, there is a large family of Magnéli phases with oxygen deficit and nominal stoichiometry ranging between MoO_2 and MoO_3 [6]. A small oxygen deficiency in substoichiometric molybdenum oxides (MoO_{3-x}, with $x \ll 1$) is reflected in appearance of crystallographic shear planes and paramagnetic centers [7]. For qualitative analysis of the structure a comparative Raman spectroscopy can be used [8]. Quantification of oxygen deficiency is possible with detailed quantitative analysis of UV–Vis spectra, particularly Intervalence Charge Transfer Transition (ICVT) related absorbance of visible light [8], and by electronic paramagnetic resonance (EPR) through the detection of Mo^{5+} species, which are directly connected with oxygen deficiency.

Thin crystalline, polycrystalline or amorphous thin films of molybdenum oxide have been extensively studied in the past for different applications. However, for some applications a powder form of nanocrystals is preferred. For example, nanocrystals can be very efficiently incorporated into polymers forming functional composites [9]. Nanosized MoO_3 in powder form has been synthesized by hydrothermal [10–12] and solvothermal [13,14] synthesis and the sonochemical method [15]. Hydrothermal and

* Corresponding author.
E-mail address: ana.varlec@ijs.si (A. Varlec).

http://dx.doi.org/10.1016/j.matchemphys.2015.12.033
0254-0584/

solvothermal synthesis usually result in nanobelts or nanowires that are tens of nanometers thick, more than 100 nm wide and tens of micrometers long [10–14]. Whiskers of similar diameter were obtained by oxidation of solvothermally synthesized MoO_2 [2]. On the other hand, smaller crystalline nanoparticles have been much more elusive and alternative approaches, such as hot-wire chemical vapor deposition (HWCVD) technique [16], are needed to prepare sub 100 nm crystalline nanoparticles or nanorods.

Since α-MoO_3 is a layered material and since layered compounds such as graphite and MoS_2 can be synthesized in a tubular geometry [17], the question is whether it is possible to synthesize α-MoO_3 in a nanotube form as well. Two successful attempts to synthesize molybdenum oxide nanotubes are known up to date: thiol assisted hydrothermal method [18] and thermal mesostructural transition of spherical micelle templates [19]. These attempts, however, do not produce α-MoO_3 nanotubes, warranting further research.

Here we present a new approach for synthesis of molybdenum oxide nanowires and nanotubes via transformation of molybdenum-sulfur-iodine nanowires. Molybdenum-sulfur-iodine nanowires of different stoichiometries are known to be suitable for transformation into MoS_2 nanotubes [20], Mo [21] and MoN [22] nanowires. Starting with the smallest so far known molybdenum-sulfur-iodine nanowires we successfully transform them into molybdenum oxide nanowires and nanotubes. These nanowires and nanotubes do adopt α-MoO_3 crystal structure. However, since they are also oxygen deficient, paramagnetic defects of both the point and crystallographic shear plane nature emerge and should be considered in possible future applications.

2. Results and discussion

2.1. X-ray diffraction (XRD)

The XRD diffractogram of the molybdenum-iodine-sulfur nanowires is shown in Fig. 1a. Its diffraction peaks were assigned according to the $Mo_6S_2I_8$ structure which consists of hexagonally arranged Mo_6L_8 (L = S, I) cluster chains growing along the [001] direction [23]. Some of the diffraction peaks are broadened to a greater extent than others. Prior to analysis of the peaks' width, the $K\alpha_2$ peaks were stripped and the remaining $K\alpha_1$ peaks were simulated with a Voigt profile (Fig. 1a), in order to obtain reliable values of peak widths (for details, see Experimental). The axes in Fig. 1a are broken in several places in order to show the simulation as clearly as possible; complete diffractograms are presented in the supplementary material (Fig. S1). Generally, XRD peaks are broadened because of both strain and small crystallite size. These two components can be discerned by assuming certain functional forms of size- and strain-induced broadening. Assuming Lorentzian broadening, both strain and size contributions can be determined from the δk(k) plot (Williamson-Hall plot [25]). If, instead, the strain contributes to Gaussian broadening (resulting in a Voigt peak), the $(\delta k/k)^2$ vs. $\delta k/k^2$ plot must be used [26]. Often, neither of these assumptions is entirely valid and therefore does not provide quantitatively correct results, but can be useful to compare similar materials or observe crystallite shape anisotropy. Since the XRD peaks in the $Mo_6S_2I_8$ diffractogram were much better fitted with the Voigt profile (Gaussian–Lorentzian broadening), we used the $(\delta k/k)^2$ vs. $\delta k/k^2$ plot (Fig. 2a). The domain size is in this case

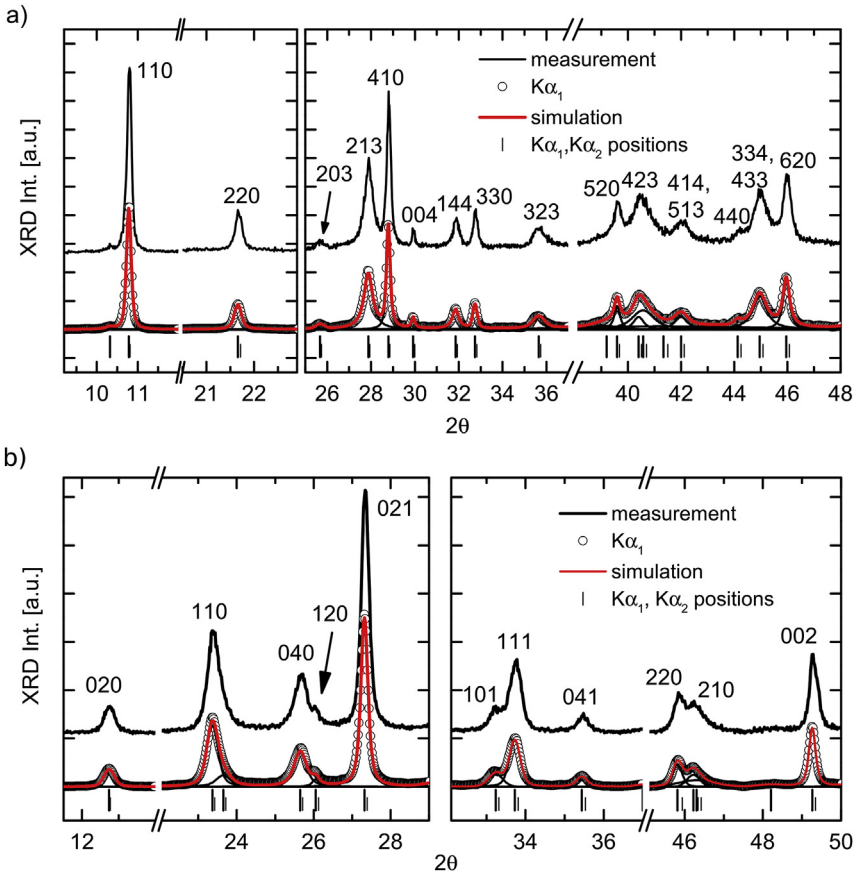

Fig. 1. XRD diffractograms. (a) $Mo_6S_2I_8$ nanowires and (b) oxidized $Mo_6S_2I_8$ nanowires. The peaks are indexed according to $Mo_6S_2I_8$ and α-MoO_3 (see text). The $K\alpha_1$ contributions were fitted with Voigt-shaped peaks. Positions of the $K\alpha_1$ and $K\alpha_2$ peaks are indicated below the graphs by long and short lines, respectively.

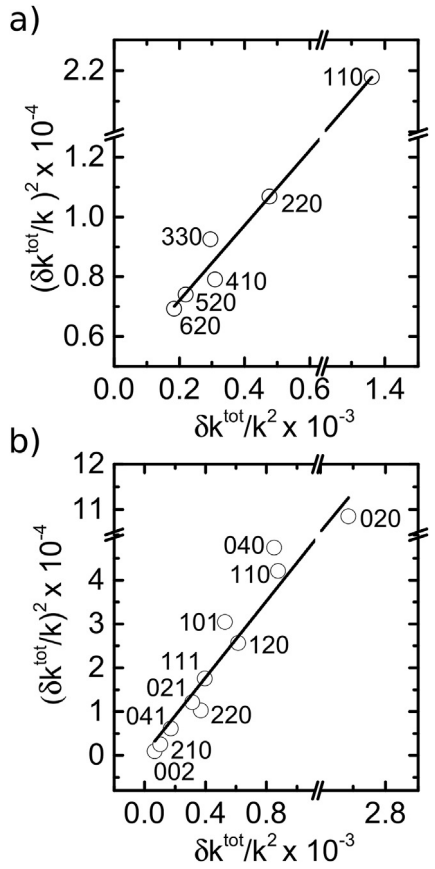

Fig. 2. Broadening of XRD peaks. Plot for separating the size and strain broadening of XRD peaks for (a) $Mo_6S_2I_8$ nanowires and (b) MoO_3 nanowires.

obtained from the slope (k_{lin}) according to $L = 2\pi/k_{lin}$ while strain (ε) is obtained from the intercept with the ordinate (n_y) according to $n_y = 4\varepsilon^2$. The peaks (hk0), including the three peaks in the [110] direction, are well described by a straight line in this plot, and the calculated domain size in the [110] direction is (50 ± 2) nm. The nonzero intercept with the ordinate indicates the presence of strain

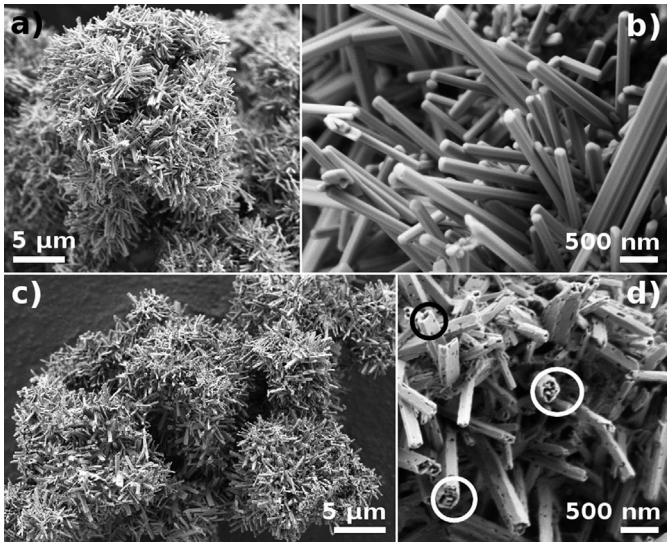

Fig. 3. SEM micrographs. (a, b) $Mo_6S_2I_8$ nanowires used as starting material; (c, d) MoO_3 nanowires and nanotubes with a hollow nanotube circled in black and porous nanowires circled in white.

in this direction. There is only one peak in the [001] direction, namely the (004). Even though its intensity is very low, it was still possible to estimate its width, which is only slightly above the instrumental broadening. A very narrow (004) peak indicates long range order, which is in agreement with the fact that $Mo_6S_2I_8$ nanowires grow in the [001] direction. Peaks in the general directions [213], [144], [323], [423], [334], are broad and interfere significantly with the background. They were not taken into account in the plot in Fig. 2a, since it is not possible to reliably determine their width. However, a very small size of crystallites cannot be the reason for their large width, since the peak (004) in the direction of growth is substantially narrower and the size in the perpendicular direction, i.e. [110], was determined to be at least 50 nm. Hence, further work is necessary to explain the effect.

In the complete diffractogram (Figure S1), two impurity-related peaks can be found in the XRD of $Mo_6S_2I_8$ nanowires, with $d = 0.615$ and $d = 0.552$ nm. The first one corresponds to either (002) reflection of MoS_2 ($d = 0.614$ nm) or MoS_2I_2 ($d = 0.611$ nm, unknown index [24]), while the identity of the other one (marked with an asterisk) is unknown.

The result of XRD analysis of the oxidized nanowires is presented in Fig. 1b. The crystalline phase matches the orthorhombic α-MoO_3 (JCPDS No. 05-0508). There are no additional peaks that would indicate the presence of a precursor material, confirming that the chosen reaction temperature was high enough not only for $Mo_6S_2I_8$ oxidation but also for the oxidation of residual molybdenum-based impurities present in the starting material. However, we notice the appearance of a broad peak at $d = 0.303$ nm (Figure S1, marked with an asterisk) that is only partially aligned with the α-MoO_3 (130) peak at 0.3007 nm. A possible explanation for this broad distribution of reflections is the presence of linear structural defects along the (130) plane. All peaks in the MoO_3 diffractogram are well fitted with symmetrical Voigt profiles (Fig. 1b). The one exception to this is the (110) peak that is more asymmetrical that can be explained with $K\alpha_2$-$K\alpha_1$ splitting and can instead be fitted with an additional peak on the right side (d = 0.3761 nm). The asymmetry cannot be explained by instrumental factors, since other peaks are not asymmetrical. It is therefore intrinsic to the structure of the nanowires, perhaps with a similar explanation as for the (130) peak. The size and strain contributions to the broadening of XRD peaks were determined from the $(\delta k/k)^2$ vs. $\delta k/k^2$ plot (Fig. 2b). All peaks are included and are reasonably well described with a straight line. Crystallite size, determined from the slope, is (14.6 ± 0.7) nm, while the value of strain is zero within the error.

2.2. Morphology studies

The SEM micrographs of $Mo_6S_2I_8$ and MoO_3 nanowires are shown in Fig. 3. The $Mo_6S_2I_8$ nanowires grow in hedgehog like structures (Fig. 3a). They are up to 2 μm long and their average width is 210 nm (Fig. 3b). Clearly visible channels running the length of the thicker nanowires indicate that these nanowires are in fact bundles of thinner wires. The latter observation is in good agreement with the estimated crystallite diameter of 50 nm obtained from the XRD peaks' width. In the HRTEM micrograph (Fig. 4) the individual chains in the [001] direction are seen. The interchain distance that can be measured from HRTEM image is 0.82 nm, which corresponds to the (110) interplane distance.

The elemental composition of the nanowires was investigated with wavelength dispersive X-ray spectroscopy (WDS). The atomic percentage of elements, measured on individual nanowires, was in agreement with the theoretical 6:2:8 ratio (37.5 at%:12.5 at%:50 at %) within the experimental error (±1 at%).

The nanowire morphology of the starting material was

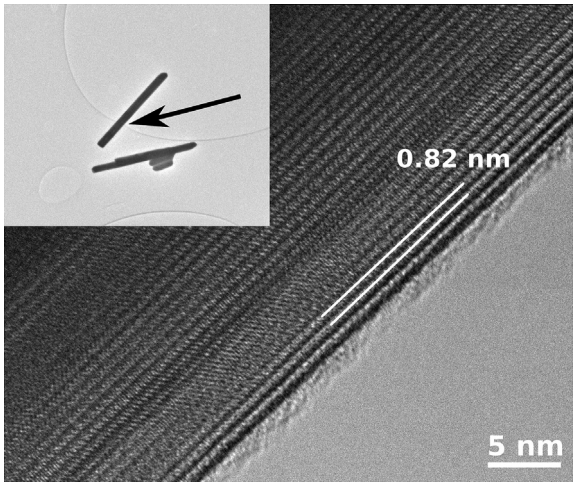

Fig. 4. TEM micrographs of $Mo_6S_2I_8$ nanowire. HRTEM at the edge of the nanowire shows individual molecular chains. The interchain distance is 0.82 nm. The inset shows the nanowire with the location imaged with HRTEM marked with an arrow.

preserved during oxidation (Fig. 3c). However, the resulting MoO_3 nanowires are polycrystalline and porous (Fig. 3d). If nanowires remained compact during the oxidation, their volume should have decreased by 35% due to the change in molar masses and densities, resulting in a 15% decrease in their diameters. But the average diameter decreased by less than 3% (distributions of nanowire diameters are shown in Figure S2). Narrow nanowires grow in semi-cylindrical shapes with a hollow interior, which is emphasized in Fig. 3d. This observation is confirmed by TEM images (Fig. 5a and b). The nanowire shown in Fig. 5a has a diameter of 130 nm. There is a large diffraction and absorption contrast between the walls and interior of the nanowire. The walls are 20 nm thick, polycrystalline, and defected, but there is a clear tendency to form a self-terminated cylindrical structure. The interior of the 200 nm wide nanowire shown in Fig. 5b, on the other hand, is filled with nanocrystals. Only a few of these crystallites form the nanotube wall; they are parallel to the electron beam. We assume that the diameter of a precursor nanowire determines whether the oxidized nanowire is filled or empty. The faceting tendency of the nanotubes is explained by a faster growth of (h0l) planes compared with the growth in the [0k0] direction and with a relatively low oxidation temperature (573 K), which enables neither intensive redistribution of material by diffusion nor eventual evaporation of MoO_3 (the evaporation temperature is above 973 K). The atomic resolution in TEM was obtained on an individual crystal (Fig. 5c) that was probably separated from a nanowire during dispersion of the nanowires in isopropanol. The diameter of this crystal is 80–90 nm, which is a typical size for crystals forming a nanowire. The interlayer distance measured on this crystal (Fig. 5d) is 3.28 nm, which can be attributed to the (011) interlayer distance of α-MoO_3.

The porosity of MoO_3 nanowires has been studied by nitrogen adsorption. The adsorption–desorption isotherm and the derived pore size distribution are shown in Fig. 6a. The amount adsorbed at the lowest attainable relative pressure, $p/p_0 = 0.015$, is nonzero, which indicates the presence of micropores. Altogether the isotherm is a combination of type I and type II, according to the IUPAC classification. Desorption hysteresis does not appear to be significant. The pore size distribution (inset of Fig. 6a) was calculated applying Barrett–Joyner–Halenda theory with the assumption of slit-shaped pores. The first peak of the distribution is at 2.4 nm. In SEM images, such small pores are obscured by the carbon coating which is necessary for obtaining the desired resolution. The distribution of macropores is broad with contributions in the whole feasible range from 5 nm up to 180 nm and an average value of 90 nm. Macropores appear to be correlated to the pores visible in SEM images in the walls of nanowires (Fig. 6b) and at the ends of nanowires and nanotubes (Fig. 6c). The calculated BET surface is 14.3 ± 0.3 m^2/g.

2.3. Raman spectroscopy

The Raman spectra of MoO_3 nanowires recorded using the green and red laser are shown in Figs. 7 and 8, respectively. For comparison, spectra taken on the α-MoO_3 single crystal are also shown. The obtained band positions for the single crystal agree with literature [27] within instrumental error and are therefore suitable for an internal standard for band positions and widths. Since band intensities depend on the orientation of the single crystal and since in the case of nanowires the spectra are averaged over all possible orientations, the band intensities of single crystals and powders cannot be directly compared.

The positons of the bands in the low power measurements of MoO_3 nanowires (Figs. 7b and 8b) match well with the band positons of the α-MoO_3 single crystal and thus confirm the XRD results. When the laser power was increased to 1.5 mW (green) and 2 mW (red), a red-shift of almost all bands was observed. The most sensitive band (160 cm^{-1}, TRM mode) was shifted by 8 cm^{-1} and by 3 cm^{-1} in the red and green laser measurements, respectively. The shift can be explained by a heating effect, because it is dependent on laser power. Heating of the sample can also affect its morphology, as demonstrated in [28]. Namely, the temperature of the sample can increase above 150 °C where nanocrystals start to coalesce, which finally influences the band position, width and intensities. The bands, which were identified as particularly sensitive to crystallite size and therefore to heating, are five translational rigid chain (TRM) modes, namely bands at 84 cm^{-1} and 98 cm^{-1}; 159 cm^{-1}; 117 cm^{-1} and 130 cm^{-1} that are polarized along the *a*, *b* and *c*-axis of the α-MoO_3, respectively.

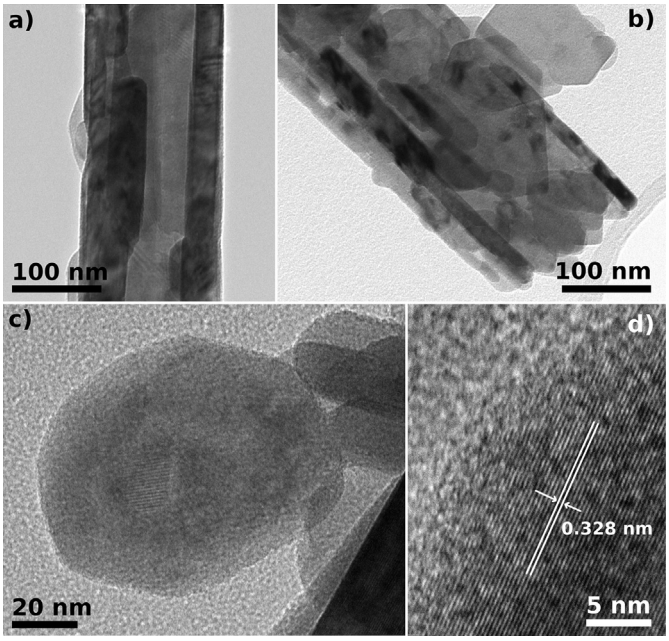

Fig. 5. TEM micrographs of MoO_3 nanowires. (a) An empty nanotube with polycrystalline walls; (b) a nanotube with encapsulated nanoparticles and nanoparticles of the same kind attached on its outer surface; (c) a thin MoO_3 flake; (d) the corresponding HRTEM image with a 0.328 nm interlayer distance.

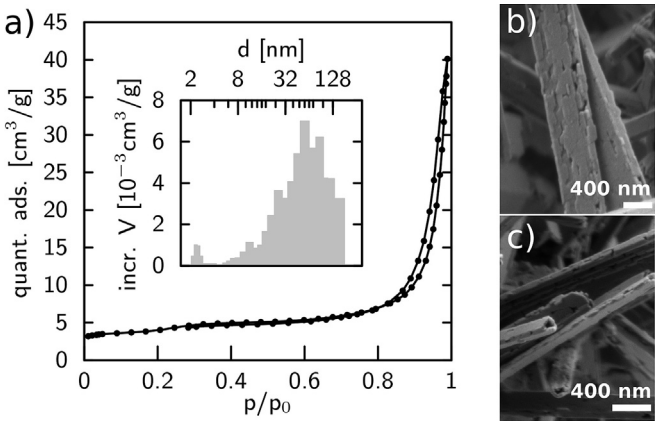

Fig. 6. Porosity. (a) Nitrogen adsorption isotherm and pore size distribution (inset) of MoO_3 nanowires and nanotubes. The distribution has a distinctive peak in the micropore region (average at 2.4 nm) and a broad peak in the macropore region (average at 90 nm). (b) SEM image of the porous structure of the nanowire wall. (c) SEM image of pores at the ends of nanowires and nanotubes.

Considering the TRM mode along the *b*-axis, the shift observed with the green laser (from 160 cm^{-1} to 157 cm^{-1}) in the present report is relatively small in comparison with the literature data [28]. Because the relative intensities of the bands were unchanged, one can conclude that no coalescence occurred in our case. The substantially larger shift when using the red laser, i.e., from 157 cm^{-1} to 149 cm^{-1}, can be explained either by greater heating or/and with the contribution of coalescence, which cannot be excluded in this case. Since the relative ratio of the TRM modes in the high-power red laser experiment is clearly different in comparison with the results using the green laser, there is a great possibility that coalescence in fact happened in the red laser measurement.

Width of bands in nanowires spectra is larger in comparison with single crystalline spectra. The reasons for this can be imperfections, such as a lower degree of crystallinity, small crystallite size and oxygen deficiency. These contributions can be separated in MoO_3 by inspecting the intensity ratio of different pairs of bands in Raman spectra [29]. Oxygen deficiency is reflected in the ratio of bands at 284 cm^{-1} and 292 cm^{-1} and the crystallite size in the ratio of bands at 130 cm^{-1} and 117 cm^{-1} [29]. In both green laser spectra of the MoO_3 nanowires, the ratio I(130)/I(117) is 2, which is in agreement with typical data for nanocrystalline MoO_3 [28,29]. Regarding oxygen deficiency, the 284 cm^{-1} and 292 cm^{-1} bands are perfectly separable in the single crystal measurement, while in the spectra of nanowires they are broadened and their strong overlap prevents reliable simulation and calculation of their intensity ratio and hence prevents conclusions on oxygen deficiency.

However, the most interesting feature in the MoO_3 nanowires' spectra is a broad band at 1004 cm^{-1}, which is clearly observed in the red laser measurement already at low power (Fig. 8b), while it is absent in the green laser measurement as well as in the red laser measurement of a single crystal. Bands at this position have been observed in mechanically activated molybdenum oxide [29,30] and two possible explanations were discussed. Firstly, a broad 1004 cm^{-1} band can be the sum of two otherwise Raman forbidden and IR active modes B_{3u} and B_{2u} centered at 1002 cm^{-1} and 1010 cm^{-1}, respectively, because in small crystallites the spectroscopic exclusion rule is weakened. The second possible explanation considers oxygen vacancies in MoO_3. That is, a 1004 cm^{-1} band can be attributed to the stretching vibration of terminal oxygen in a tetrahedron with missing ternary oxygen. The intensity of this signal was proven to be strongly dependent on the excitation light, since red excitation light fulfills the resonant Raman condition. The intensity of the 1004 cm^{-1} band in the MoO_3 nanowires' spectra is clearly dependent on the excitation wavelength in this manner, therefore one can conclude that this signal is likely due to oxygen vacancies.

2.4. Electron paramagnetic resonance

An EPR spectrum of MoO_3 nanowires recorded at 80 K is shown in Fig. 9. The observed g-factor values are typical for Mo^{5+} centers in the reduced MoO_3 [7,31,32]. The spectrum was simulated as a sum of two different Mo^{5+} centers, a narrow one with a resolved hyperfine structure (center I) and a broad one (center II). A homogeneously broadened Lorentzian lineshape was used for both center types. The values of simulation parameters are presented in Table 1. Center I is anisotropic with g values of $g_y = 1.954$, $g_x = 1.941$ and $g_z = 1.865$. Using values of hyperfine coupling constants for the ^{95}Mo and ^{97}Mo nuclear spin $I = 5/2$ provided in Table 1, the main characteristics of the EPR spectrum are successfully reproduced, although it is not entirely possible to capture some of the subtle hyperfine details. For instance, the highest m_I transitions can be resolved more clearly compared to the lower m_I transitions, most likely due to the dynamic effects that are responsible for m_I dependent linewidth broadening (see e.g., Reference [33]). Paramagnetic centers similar to center I in present study have been assigned to pentacoordinate Mo^{5+} in the vicinity of an oxygen vacancy in vacuum reduced MoO_3 (see Table 1). In comparison, the center in the H_2 reduced MoO_3 sample has a considerably higher g_z value as a result of H^+ effect on MoO_6 octahedral structure.

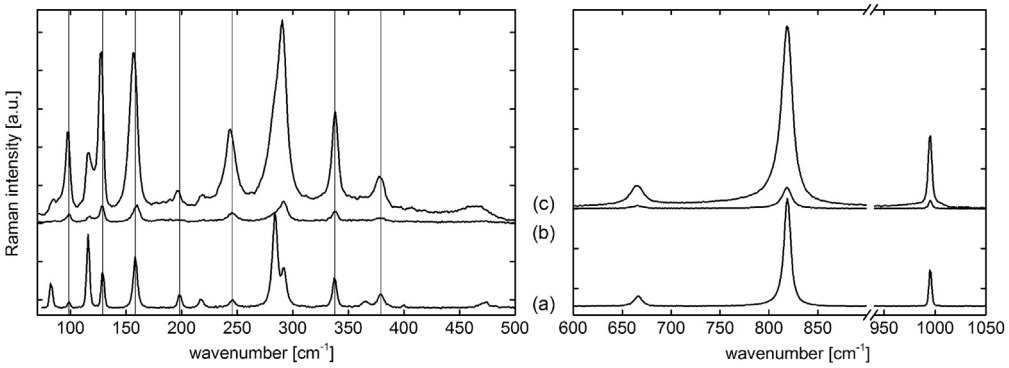

Fig. 7. Raman spectra recorded with the green laser. (a) MoO_3 single crystal; (b) MoO_3 nanowires and nanotubes at low power; (c) MoO_3 nanowires and nanotubes at high power. Vertical lines are centered at the single crystal bands to emphasize the slight band shifts of the nanowires.

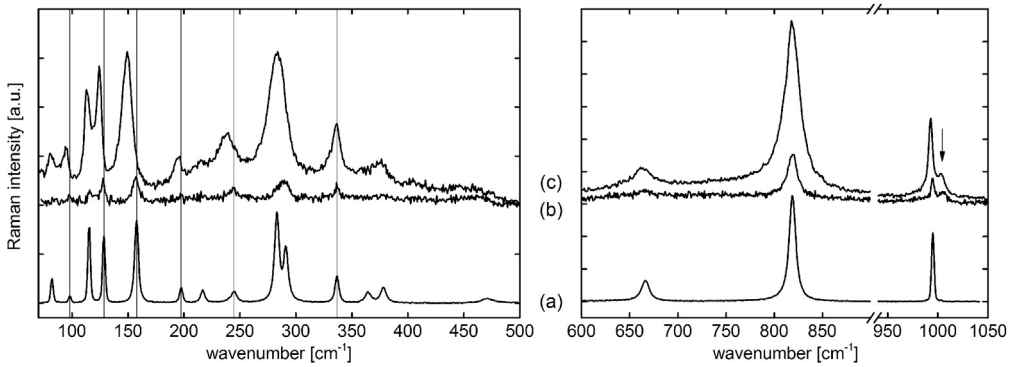

Fig. 8. Raman spectra recorded with the red laser. (a) MoO_3 single crystal; (b) MoO3 nanowires and nanotubes recorded with low power; (b) MoO_3 nanowires and nanotubes recorded with high power. The intensity of spectrum (a) is divided by 20 for greater clarity. Vertical lines are centered at the single crystal bands to emphasize the large band shift of the nanowires. The 1004 cm^{-1} band is marked with an arrow.

Component I thus clearly confirms the presence of oxygen vacancies in the MoO_3 nanowires and thus fully corroborate the Raman data.

Center II is simulated with an average g-factor of 1.910. Its linewidth is almost an order of magnitude larger than that of center I thus completely obscuring the hyperfine interaction. Since the large broadening is likely due to magnetic interactions one can deduce that the paramagnetic centers of the type II are exchange coupled. Strong magnetic exchange interaction is possible within paramagnetic centers that are in close proximity. One can thus conclude that Mo^{5+} centers of type II belong the crystal shear planes, where the defects are ordered and in close proximity.

The quantity of paramagnetic centers can be estimated by comparing the EPR signal intensity to the intensity of a standard sample. We have obtained that (0.05 ± 0.01) % of all Mo are in the Mo(V) state. Assuming that each Mo(V) is correlated with one oxygen vacancy and that there are no further reduced Mo states (since Mo(IV) for instance, is EPR silent), the stoichiometry of MoO_{3-x} nanowires is $MoO_{2.998}$.

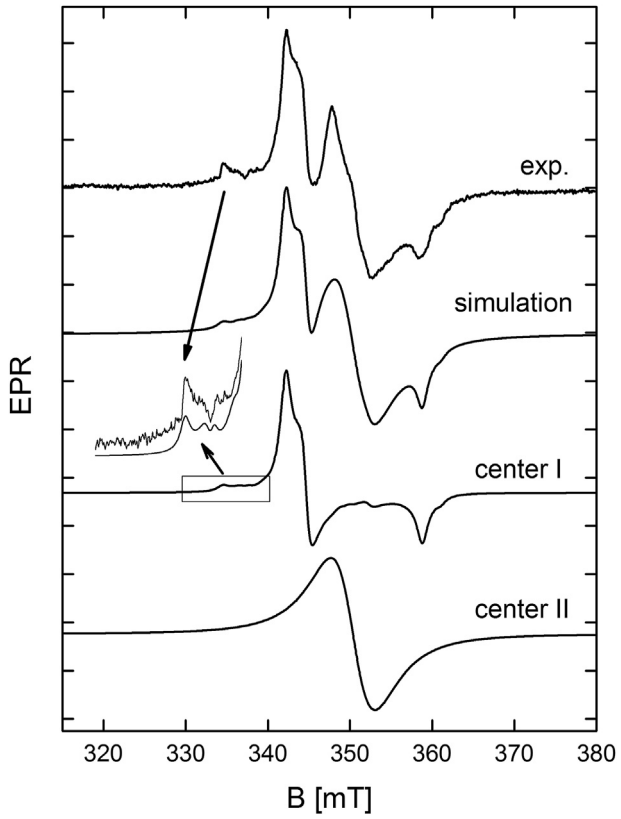

Fig. 9. EPR spectrum of the MoO_3 nanowires. The measured EPR spectrum and simulation using two components, i.e. centers I and II (parameters in Table 1) are shown. The inset shows a simulation of center I with a narrower linewidth (1 mT) emphasizing the hyperfine features in the proximity of g_x and the corresponding part of the experimental curve.

3. Conclusions

We synthesized MoO_3 nanowires and nanotubes from $Mo_6S_2I_8$ nanowires via oxidation in air. Nanowire morphology of this starting material is preserved during oxidation, but the resulting MoO_3 nanowires are polycrystalline and porous. SEM and TEM show that they have grown into semi-cylindrical shape with hollow or partially filled interior depending on the diameter of the precursor nanowire. The orthorhombic α-MoO_3 phase has been determined from XRD data and Raman spectroscopy. The porosity of the nanowires and faceting tendency of the nanotubes are explained by the density and molar mass change during oxidation and the layered structure of α-MoO_3, respectively. Upon laser induced heating the Raman bands have shifted, and for red laser excitation the coalescence of nanoparticles could not be excluded. An additional broad Raman band at 1004 cm^{-1} was clearly observed and attributed to missing oxygen. EPR investigation showed that the extent of oxygen deficiency is large enough for the appearance of crystal shear planes typical for Magnéli phases.

4. Experimental

The molybdenum-sulfur-iodine nanowires were synthesized under chemical transport reaction conditions in evacuated quartz ampules (10^{-4} Pa) from molybdenum (Aldrich 99.9%) and sulfur (Aldrich 99%) powder and iodine beads (Sigma–Aldrich Reagent-plus® grade) in the molar ratio 6:2:11.6. The reaction lasted for 48 h. The temperature gradient was 5.5 K/cm, the highest and lowest temperatures being 1133 K and 1010 K, respectively. Heating rate for the cold and hot zones were 17.4 K/h and 14.8 K/h, respectively, and cooling rates were twice as fast. The obtained nanowires were rapidly heated to 573 K and oxidized for 25 h in air in order to transform them into molybdenum oxide nanowires.

Powder X ray diffraction (XRD) of the synthesized materials was performed at room temperature with D4 Endeavor diffractometer (Bruker AXS) using a quartz monochromator Cu Kα radiation source

Table 1.
EPR parameters. EPR parameters from simulations of the MoO_3 nanowires' spectra and some relevant data from the literature.

Center	g_x, g_y, g_z			A [MHz]		γ [mT]	Assignment	References
I	1,941	1,954	1,865	83	24	1,56		This work
II		1,9095				9,22		This work
	1,943	1,957	1,864	89	156		Mo^{5+} in vicinity of an oxygen vacancy; vacuum reduced MoO_3	[31] and Ref. therein
	1,946	1,9562	1,8805	174			Mo^{5+} in H_2 reduced MoO_3	[34]
	1,933	1,910					Mo^{5+} in shear structures	[31]
	1,936	1,899					Mo^{5+} in shear structures	[32]

($\lambda = 0.1541$ nm) and a Sol-X dispersive detector. The range of 2θ was chosen from 10° to 60° with a step size of 0.02° and collection time of 3 s. The samples were rotated during the measurements at 6 rpm. $K\alpha_2$ peaks were stripped using penalized likelihood method and composite link method (PCLM) [35]. Peaks were fitted with Voigt profile, implemented in the fityk software [36]. The instrumental broadening was subtracted via $B_{tot} = B_{meas}\text{-}(B_{inst}/B_{meas})\ B_{instr}$ [26]. For calculations, FWHM was used instead of integral breadth, since the former is less sensitive to background compared to the latter.

The morphology of the nanowires was investigated using field emission scanning electron microscope (SEM), Supra 36 VP, Carl Zeiss and high resolution 200 keV Jeol 2010 F field emission transmission electron microscope (HRTEM). The samples for the HRTEM were prepared by sonication in ethanol for 20 min and drop casting of the suspension onto a holey-carbon Cu grid. Elemental analysis was done with JEOL JSM7600 F, equipped with wavelength dispersive X-ray spectroscopy (WDS) unit. Single crystals of 2H–MoS_2 and MoI_2 were used as standards.

Nitrogen physisorption measurements were carried out at 77 K using Micromeritics Tristar 3000 volumetric adsorption analyzer. Before the measurement, the sample was outgassed for 6 h at 110 °C in the port of the adsorption analyzer. The specific surface area was calculated using the standard BET method. Pore size distribution was estimated using the BJH method including the whole pressure range.

Raman spectra of oxidized nanowires were recorded with WITec Alpha 300 scanning confocal Raman microscope using two excitation wavelengths: 532.3 nm and 632.8 nm. Samples in powder form were manually pressed to obtain relatively flat surface suitable for mapping. Laser light was focused with a 20 × objective. The power of the laser beam at the sample position was 0.1 mW and 1.5 mW for the green laser light, and 0.5 mW and 2 mW for the red laser light. Spectra were averaged over a 30 μm square region and were therefore simultaneously averaged over all possible orientations of the nanocrystals forming the nanowires. For comparison, Raman spectra of α-MoO_3 single crystal at low powers were also recorded.

EPR spectra of oxidized nanowires were recorded by an EPR spectrometer equipped with a Varian E-101 microwave bridge and a Varian TE_{102} resonance cavity. Spectral simulations were carried out using Easy Spin software [37]. The standard used for quantitative EPR was $CuSO_4 \times 5H_20$.

Acknowledgments

The authors thank Janez Jelenc for synthesis of the nanowires, Matjaž Mazaj and Mojca Opresnik for nitrogen adsorption measurement, Maja Koblar for WDS measurements and Goran Dražić for HRTEM images. Work was financially supported by Slovenian Research Agency through contracts P1-0099 and 1000-11-310181.

Appendix A. Supplementary data

Supplementary data related to this article can be found at http://dx.doi.org/10.1016/j.matchemphys.2015.12.033.

References

[1] J. Meyer, R. Khalandovsky, P. Görrn, A. Kahn, MoO_3 films spin-coated from a nanoparticle suspension for efficient hole-injection in organic electronics, Adv. Mater 23 (2011) 70–73.
[2] W.-S. Kim, H.-C. Kim, S.-H. Hong, Gas sensing properties of MoO_3 nanoparticles synthesized by solvothermal method, J. Nanoparticle Res. 12 (2010) 1889–1896.
[3] Y.A. Yang, Y.W. Cao, B.H. Loo, J.N. Yao, Microstructures of electrochromic MoO_3 thin films colored by injection of different cations, J. Phys. Chem. B 102 (1998) 9392–9396.
[4] R.S. Devan, R.A. Patil, J.-H. Lin, Y.-R. Ma, One-dimensional metal-oxide nanostructures: recent developments in synthesis, characterization, and applications, Adv. Funct. Mater 22 (2012) 3326–3370.
[5] C. Zollfrank, K. Gutbrod, P. Wechsler, J.P. Guggenbichler, Antimicrobial activity of transition metal acid MoO_3 prevents microbial growth on material surfaces, Mater. Sci. Eng. C 32 (2012) 47–54.
[6] L. Kihlborg, Studies on molybdenum oxides, Acta Chem. Scand. 13 (1959) 954–962.
[7] G. Mestl, N.F.D. Verbruggen, E. Bosch, H. Knözinger, Mechanically activated MoO_3. 5. Redox Behavior, Langmuir 12 (1996) 2961–2968.
[8] M. Dieterle, G. Mestl, G. Weinberg, Raman spectroscopy of molybdenum oxides. Part I. Structural characterization of oxygen defects in MoO_{3-x} by DR UV/VIS, Raman and X.ray diffraction, Phys. Chem. Chem. Phys. 4 (2002) 812–821.
[9] V. Domenici, M. Conradi, M. Remškar, M. Viršek, B. Zupančič, A. Mrzel, et al., New composite films based on MoO_{3-x} nanowires aligned in a liquid single crystal elastomer matrix, J. Mater. Sci. 46 (2011) 3639–3645.
[10] X.-L. Li, J.-F. Liu, Y.-D. Li, Low-temperature synthesis of large-scale single-crystal molybdenum trioxide (MoO_3) nanobelts, Appl. Phys. Lett. 81 (2002) 4832.
[11] X.W. Lou, H.C. Zeng, Hydrothermal synthesis of α-MoO_3 nanorods via acidification of ammonium heptamolybdate tetrahydrate, Chem. Mater 14 (2002) 4781–4789.
[12] C.V. Subba Reddy, E.H. Walker, C. Wen, S. Mho, Hydrothermal synthesis of MoO_3 nanobelts utilizing poly(ethylene glycol), J. Power Sources 183 (2008) 330–333.
[13] G.R. Patzke, A. Michailovski, F. Krumeich, R. Nesper, J.-D. Grunwaldt, A. Baiker, One-step synthesis of submicrometer fibers of MoO_3, Chem. Mater 16 (2004) 1126–1134.
[14] J. Song, X. Ni, D. Zhang, H. Zheng, Fabrication and photoluminescence properties of hexagonal MoO_3 rods, Solid State Sci. 8 (2006) 1164–1167.
[15] C.V. Krishnan, J. Chen, C. Burger, B. Chu, Polymer-assisted growth of molybdenum oxide whiskers via a sonochemical process, J. Phys. Chem. B 110 (2006) 20182–20188.
[16] S.-H. Lee, Y.-H. Kim, R. Deshpande, P.A. Parilla, E. Whitney, D.T. Gillaspie, et al., Reversible lithium-ion insertion in molybdenum oxide nanoparticles, Adv. Mater 20 (2008) 3627–3632.
[17] M. Remškar, Inorganic nanotubes, Adv. Mater 16 (2004) 1497–1504.
[18] S. Hu, X. Wang, Single-walled MoO_3 nanotubes, J. Am. Chem. Soc. 130 (2008) 8126–8127.
[19] B.P. Bastakoti, M. Imura, Y. Nemoto, Y. Yamauchi, Synthesis of MoO_3 nanotubes by thermal mesostructural transition of spherical triblock copolymer micelle templates, Chem. Commun. 48 (2012) 12091.
[20] M. Virsek, M. Krause, A. Kolitsch, A. Mrzel, I. Iskra, S.D. Škapin, et al., The transformation pathways of $Mo_6S_2I_8$ nanowires into morphology-selective MoS_2 nanostructures, J. Phys. Chem. C 114 (2010) 6458–6463.
[21] A. Kovic, A. Znidarsic, A. Jesih, A. Mrzel, M. Gaberscek, A. Hassanien, A novel facile synthesis and characterization of molybdenum nanowires, Nanoscale Res. Lett. 7 (2012) 1–7.
[22] J. Buh, A. Kovič, A. Mrzel, Z. Jagličić, A. Jesih, D. Mihailovic, Template synthesis of single-phase δ3-MoN superconducting nanowires, Nanotechnology (2014) 25, 025601.
[23] C. Perrin, M. Sergent, A new family of monodimensional compounds with octahedral molybdenum clusters: $Mo_6X_8Y_2$ (X=Halogen, Y=Chalcogen),

J. Chem. Res. Synop. 1983 (1983) 38–39.
[24] D.V. Drobot, V.V. Starkov, E.A. Pisarev, Interaction of molybdenum diiodide with sulfur, Zhurnal Neorganicheskoj Khimii 30 (1985) 1670–1673.
[25] S. Safa, R. Azimirad, S. Safalou Moghaddam, M. Rabbani, Investigating on photocatalytic performance of CuO micro and nanostructures prepared by different precursors, Desalination Water Treat. (2015) 1–9.
[26] C.E. Krill, R. Haberkorn, R. Birringer, Specification of microstructure and characterization by scattering techniques, in: H.S. Nalwa (Ed.), Nanostructured Mater, Nanotechnol, San Diego, 1999. Handb.
[27] M.A. Py, K. Maschke, Intra- and interlayer contributions to the lattice vibrations in MoO_3, Phys. B. C. 105 (1981) 370–374.
[28] J.V. Silveira, L.L. Vieira, J.M. Filho, A.J.C. Sampaio, O.L. Alves, A.G. Souza Filho, Temperature-dependent Raman spectroscopy study in MoO_3 nanoribbons: temperature-dependent Raman spectroscopy in MoO_3 nanoribbons, J. Raman Spectrosc. 43 (2012) 1407–1412.
[29] G. Mestl, T.K.K. Srinivasan, H. Knözinger, Mechanically activated MoO_3. 3. Characterization by vibrational spectroscopy, Langmuir 11 (1995) 3795–3804.
[30] G. Mestl, N.F.D. Verbruggen, F.C. Lange, B. Tesche, H. Knözinger, Mechanically activated MoO_3. 4. In situ characterization of physical mixtures with Al_2O_3, Langmuir 12 (1996) 1817–1829.
[31] M. Labanowska, Paramagnetic defects in MoO_3 -revisited, Phys. Chem. Chem. Phys. 1 (1999) 5385–5392.
[32] K. Dyrek, M. Labanowska, Electron paramagnetic resonance investigation of the paramagnetic centres in polycrystalline MoO_3, J. Chem. Soc. Faraday Trans. 87 (1991) 1003–1009.
[33] J.A. Weil, J.R. Bolton, Relaxation Times, Linewidths and Spin Kinetic Phenomena. Electron Paramagn. Reson, John Wiley & Sons, Inc., 2006, pp. 301–356.
[34] M. Labanowska, Electron paramagnetic resonance study of interaction between MoO_3 and propene, Phys. Chem. Chem. Phys. 2 (2000) 3307–3311.
[35] J.J. de Rooi, N.M. van der Pers, R.W.A. Hendrikx, R. Delhez, A.J. Böttger, P.H.C. Eilers, Smoothing of X-ray diffraction data and $K\alpha_2$ elimination using penalized likelihood and the composite link model, J. Appl. Crystallogr. 47 (2014) 852–860.
[36] M. Wojdyr, Fityk: a general-purpose peak fitting program, J. Appl. Crystallogr. 43 (2010) 1126–1128.
[37] S. Stoll, A. Schweiger, EasySpin, a comprehensive software package for spectral simulation and analysis in EPR, J. Magn. Reson 178 (2006) 42–55.